

Accepted manuscript

Tensile strength distribution of all-oxide ceramic matrix mini-composites with porous alumina matrix phase

Henning Richter, Piet W. M. Peters

[doi:10.1016/j.jeurceramsoc.2016.05.012](https://doi.org/10.1016/j.jeurceramsoc.2016.05.012)

To appear in: *Journal of the European Ceramic Society*



© 2016. This is a PDF file of an unedited manuscript that has been accepted for publication. Licensed under the Creative Commons BY-NC-ND 4.0 license (<http://creativecommons.org/licenses/by-nc-nd/4.0/>).

Tensile strength distribution of all-oxide ceramic matrix mini-composites with porous alumina matrix phase

Henning Richter^{a,*}, Piet W. M. Peters^a

^a*Institute of Materials Research, German Aerospace Center (DLR), Linder Hoehe, 51147 Köln, Germany*

Abstract

The mechanical behaviour of all-oxide ceramic matrix mini-composites with porous alumina matrix phase was investigated by performing uniaxial tensile tests on specimens with different gauge lengths. The specimens were fabricated from NextelTM 610 fibres by slurry infiltration and subsequent sintering at 1300 °C for one hour.

The stress-strain curves of the tested mini-composites revealed that the porous alumina matrix phase accumulates damage with increasing tensile load, but continues to contribute to the mini-composites' tensile stiffness until ultimate failure occurs. A dependence of the tested mini-composites' axial tensile strength on gauge length was not observed. The mean stress in the fibres at mini-composite failure was found to decrease with increasing matrix volume fraction, indicating that the cause of ultimate failure of the mini-composites can be attributed to the propagation of matrix cracks.

Keywords: Ceramic-matrix composites (CMCs), Mechanical testing, Tensile strength, Statistical properties, Microstructure

1. Introduction

Owing to their fracture toughness, heat and oxidation resistance, as well as low specific weight, all-oxide Ceramic Matrix Composites (CMCs), which typically consist of alumina or aluminosilicate fibre bundles embedded in a porous, alumina- or aluminosilicate-based matrix, are promising materials

*Corresponding author. Tel.: +49 2203 601-2430

Email address: henning.richter@dlr.de (Henning Richter)

for high-temperature applications under oxidizing conditions. The non-linear structural behaviour exhibited by all-oxide CMC components with multi-directional fibre orientation under fibre-nonparallel mechanical loading results from the interplay of damage and failure processes acting at several material length scales. The CMC components' overall performance is strongly influenced by the mechanical properties of the unidirectional fibre bundles, which constitute the smallest repetitive mechanical entity discernible in all-oxide CMCs [1, 2].

Generally, the mechanical behaviour of the fibre bundles in all-oxide CMCs differs fundamentally from that found in conventional, polymer-based unidirectional composites. In the latter, the ductile matrix phase exhibits high strain-to-failure but low strength. The embedded fibres primarily stiffen and reinforce the polymer matrix. The axial tensile strength of the fibre bundles depends on the statistical strength properties of the fibres, the shear properties of the matrix phase and the fibre-matrix bond strength [3–7]. The damage process under tensile loading is characterized by matrix yielding, successive fibre rupture and load transfer between fractured and intact fibre segments [6, 8].

In all-oxide CMCs, however, the brittle porous matrix phase generally has low strain-to-failure and comparatively low strength [9, 10]. The embedded fibres primarily toughen the porous matrix phase [11, 12]. The axial tensile strength of the fibre bundles in a ceramic matrix is commonly reported to be influenced by fibre strength statistics [13–16] and fibre-matrix debonding resistance [1, 2, 17–20].

While a multitude of micromechanical models describing the damage and failure behaviour of CMCs have been described in literature [21–32], published experimental data on the strength properties of unidirectional ceramic fibre bundles embedded in a brittle ceramic matrix, so-called ceramic matrix mini-composites, is scarce [28, 33–35], especially for all-oxide ceramic matrix mini-composites [36].

This paper aims at contributing to the experimental background by reporting on the results of uniaxial tensile tests on all-oxide ceramic matrix mini-composites consisting of NextelTM 610 alumina fibres [37] embedded in an alumina matrix phase with more than 30 vol% matrix porosity. A total of 90 mini-composites with three different gauge lengths were tested to investigate whether the mini-composites' axial tensile strength exhibits a dependence on gauge length. The obtained strength data and the stress-strain curves of the tested mini-composites were analysed to evaluate the mini-composites' damage and failure behaviour.

2. Experimental

2.1. Specimen preparation

The investigated ceramic matrix mini-composites were manufactured using a NextelTM 610 fibre roving with a linear mass density of 3000 den, which corresponds to a nominal filament count of 750 [37], and an aqueous ceramic slurry of α -Al₂O₃ particles with an average particle size of approximately 200 nm prepared from PURAL[®] boehmite powder [38, 39]. During manufacturing of the mini-composites, the as-received fibre roving was passed through a furnace to remove the organic sizing, infiltrated with the ceramic slurry and fed through a deflector with an opening of 1 mm in diameter to remove excess slurry. This manufacturing procedure, which is schematically shown in Fig. 1(a), is similar to the standard processing route of WHIPOX[®] components [40]. The infiltrated roving was manually cut into 18 bundle sections with lengths varying from approximately 800 mm to 1400 mm, which were then air dried for several hours. From each of the six shortest bundle sections, one set, and from each of the remaining 12 bundle sections, two sets of three tensile test specimens with nominal gauge lengths $l_g = 50$ mm, 125 mm and 250 mm were cut, yielding a total of $n = 30$ specimens per gauge length. All specimens were sintered for one hour at a temperature of 1300 °C in air. The resulting matrix phase exhibits high porosity and more than 99.8 wt% alumina content.

After sintering, the mass and overall length of each specimen were recorded. Using Archimedes' principle, the density of one specimen from each of the 18 bundle sections was determined. This density was assumed to be representative for all specimens cut from the respective bundle section. With the known mass, density and overall length, the volume V and the average cross-sectional area A_c of each mini-composite specimen were computed.

The specimens were glued on 2 mm thick aluminium mounting tabs using a two-part epoxy adhesive, cf. Fig. 1(b), in order to facilitate handling and clamping, as well as to achieve, during mechanical testing, a gradual transfer of load from the clamped mounting tab to the specimen through shearing of the glue layer. The length of each gripping area was 40 mm.

2.2. Mechanical testing

Uniaxial tensile tests were carried out according to ASTM standards C1275-10 and C1557-03 [41, 42] on a dual-column Instron 5566A testing machine equipped with a 500 N load cell in a controlled environment at a

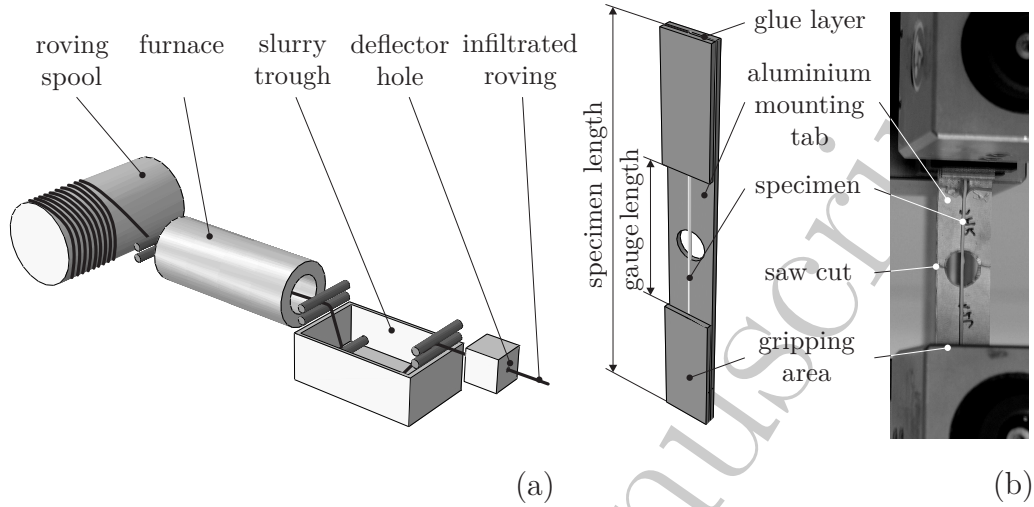


Figure 1: Schematic processing route of unidirectional all-oxide ceramic matrix mini-composites (a), mounting tab geometry used for mechanical testing (b).

temperature between 21 °C and 22 °C, a relative humidity between 50 % and 60 % and 984 hPa to 997 hPa ambient pressure.

During each test cycle, the mounted test specimen was positioned between the serrated grip faces and carefully aligned with marks on the grips in order to prevent spurious bending or torsion of the specimen. After clamping, the mounting tab was cut at the central drill-hole, cf. Fig. 1(b). Although care was taken to avoid damaging the fibre bundle surface, three specimens were destroyed during this process. Each tensile test was conducted at a constant nominal strain rate of approximately 10^{-4} s^{-1} to achieve fracture of the specimen within 20 s [42]. In the course of each test, the force F and the cross-head displacement u were recorded.

The cross-head displacement was used to estimate the specimens' tensile strain ε : to compensate for the compliance of the grips and other components in the load train, an effective gauge length l_e was determined from an additional tensile test on an as-received fibre roving embedded in epoxy resin, with a nominal gauge length of 50 mm. Neglecting the comparatively low Young's modulus of the epoxy matrix, the gauge length of the specimen was adjusted during analysis of the test result until the slope of the linear region of the stress-strain curve matched the known Young's modulus of the fibres [37], yielding an effective gauge length of $l_e = 59.18 \text{ mm}$. Assuming the added compensation of 9.18 mm to be independent of the specimens' nominal gauge

length, the effective gauge lengths l_e of the longer specimens were determined to be 134.18 mm and 259.18 mm, respectively.

2.3. Microscopy

After mechanical testing, a polished cross-section was prepared from each of the 18 bundle sections at a random location in order to determine the actual number n_f of fibres in the tested specimens. The individual fibres were counted on digital images obtained by scanning electron microscopy. Assuming the number of fibres to remain constant along the length of a bundle section, the fibre volume fraction φ and the matrix porosity ϕ_m of each specimen were computed from the number of fibres and the specimen length and volume for an average fibre diameter of $11.8\ \mu\text{m}$ [43]. The digital images of polished cross-sections were further submitted to area measurements, using the ImageJ image analysis toolbox [44].

3. Results and discussion

3.1. Specimen microstructure

Actual fibre counts n_f of the 18 bundle sections ranged from 633 to 748. The fluctuation in fibre count is attributed to the rupture of individual filaments during manufacturing. The resulting fibre volume fraction φ of the mini-composites was found to vary from 12.8 vol% to 44.1 vol%, and matrix porosity ϕ_m was found to be in the range of 33.1 vol% to 43.1 vol%.

The digital area measurements confirmed the results derived from Archimedes density measurements, indicating that the variation in average cross-sectional area A_c along the length of the individual bundle sections is minimized by using the deflector to remove excess matrix slurry. However, a variation in diameter among different bundle sections occurred despite using the deflector, and some bundle sections exhibit a diameter that is notably smaller than the deflector opening.

3.2. Screening for outlying data

Due to the pronounced scatter in measured load at failure data, prior to further analyses, the test results for each nominal gauge length were separately scanned for erroneous, outlying data using the maximum normed residual criterion [45–47]. For each set of load at failure data F_{b_i} , $i = 1, 2, \dots, n$, where the sample size n indicates the number of successfully tested specimens,

cf. Section 2.2, the maximum normed residual T was computed according to the relation

$$T = \frac{\max |F_{b_i} - \overline{F_b}|}{s}. \quad (1)$$

Here, $\overline{F_b} = n^{-1} \sum_{i=1}^n F_{b_i}$ is the sample mean and s denotes the sample standard deviation

$$s = \sqrt{\frac{1}{n-1} \sum_{i=1}^n (F_{b_i} - \overline{F_b})^2}. \quad (2)$$

In order to determine whether the datum F_{b_i} associated with the maximum normed residual T was an outlier or not, T was compared with a critical value C at a significance level of 0.05. The computed maximum normed residuals and the corresponding critical values for the data sets of each gauge length are listed in Table 1.

Table 1: Maximum normed residual test of normally distributed load at failure data for significance level of 0.05 (* values taken from [46]).

nominal gauge length l_g [mm]	sample size n	sample mean $\overline{F_b}$ [N]	sample std. deviation s [N]	max. normed residual T	critical value C
50	29	56.5	12.8	1.728	2.730*
125	30	50.9	13.4	2.063	2.745*
250	28	49.7	10.8	2.188	2.714*

At the significance level of 0.05, all maximum normed residuals fall below their respective critical values, indicating that the sets of test results do not contain outlying data.

3.3. Axial tensile strength

The axial tensile strength σ_{c_b} of a mini-composite is defined as the quotient of its maximum load at failure F_b and its average cross-sectional area A_c ,

$$\sigma_{c_b} = \frac{F_b}{A_c}. \quad (3)$$

The range of tensile strength data of successfully tested specimens is illustrated by box plots in Fig. 2: each box represents data that fall between the first and third quartile of the strength distribution for the corresponding gauge length, the median being marked by a bold horizontal line. Vertical lines characterize the lowest and the highest datum still within the interval defined by 1.5 times the interquartile range of the lower quartile to 1.5 times the interquartile range of the upper quartile. Data exceeding 1.5 times the interquartile range above the upper quartile are excluded from further analysis and denoted by circles [48]. The mean tensile strength of the reduced data set is marked by a bold dashed line.

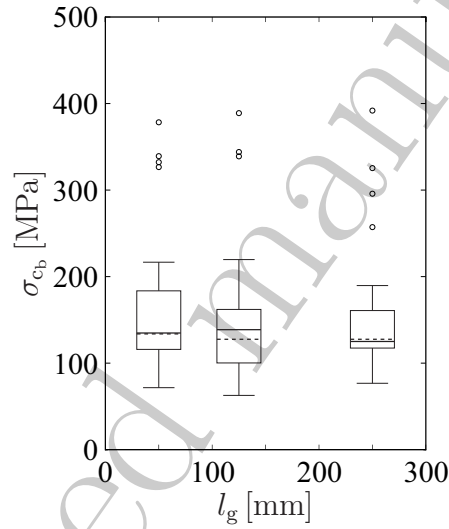


Figure 2: Box plots of the mini-composites' axial tensile strength data σ_{cb} for different nominal gauge lengths l_g .

It can be seen from Fig. 2 that the three distributions of tensile strengths cover a similar range. Excessively high strength values present in each distribution are attributed to specimens with fibre volume fractions φ exceeding 40 vol%. Fig. 2 further shows that the strength distribution for specimens with 250 mm gauge length exhibits a smaller interquartile range, which may be explained by the increased lateral mobility of the long gauge length sections that facilitates reorientation of the specimens towards the loading axis and limits the spread of measured load at failure data. Besides, the three strength distributions are skewed, which corresponds to the fluctuations in fibre volume fraction. The means of the strength data distributions read 134.2 MPa (standard deviation 33.6 MPa) for 50 mm gauge length, 127.6 MPa

(40.8 MPa) for 125 mm gauge length and 127.6 MPa (28.0 MPa) for 250 mm gauge length.

3.4. Stress-strain behaviour

A stress-strain curve for each of the tested unidirectional mini-composites was obtained by dividing the recorded data of force F and cross-head displacement u by the mini-composite's average cross-sectional area A_c and its effective gauge length l_e , respectively. The tensile Young's modulus E_c of each mini-composite was determined from the slope of the linear region of the stress-strain curve, yielding mean values of 124.7 GPa (standard deviation 42.1 GPa) for 50 mm gauge length, 122.8 GPa (41.7 GPa) for 125 mm gauge length and 133.2 GPa (36.2 GPa) for 250 mm gauge length.

The slopes of the ascending stress-strain curves of the mini-composites predominantly exhibit a gradual decrease prior to reaching the ultimate tensile stress, as exemplarily shown in Fig. 3(a), which is attributed to cumulative matrix micro-cracking and opening of cracks already present in the porous matrix phase due to fibre-constrained matrix shrinkage during sintering. This observation was confirmed by optical microscopy of several tested mini-composites, which revealed multiple irregularly-spaced matrix cracks oriented perpendicular to the mini-composites' longitudinal axis, cf. Fig. 4.

However, the stress-strain curves do not show the characteristics of matrix crack saturation, fibre-matrix debonding and fibre-dominated failure that are observed on unidirectional CMCs containing fibres with (fugitive) coatings after exceeding the tensile strength σ_{m_b} of the matrix phase, as illustrated with Fig. 3(b). The slopes of the stress-strain curves of the damaged all-oxide mini-composites, in particular, are steeper than the slopes attributed to a mere stiffness contribution φE_f of the fibres alone [49–51]. It can therefore be assumed that the damaged matrix phase continues to carry load until the ultimate tensile stress of the mini-composites is reached.

3.5. Damage and failure behaviour

3.5.1. Fibre stress at failure

To evaluate the effect of the damaged matrix phase on the mini-composites' tensile strength, the mean stress σ_f in the fibres at the point of failure of the mini-composites was determined using the equation

$$\sigma_f = \frac{\sigma_{c_b} - (1 - \varphi)\sigma_m}{\varphi}. \quad (4)$$

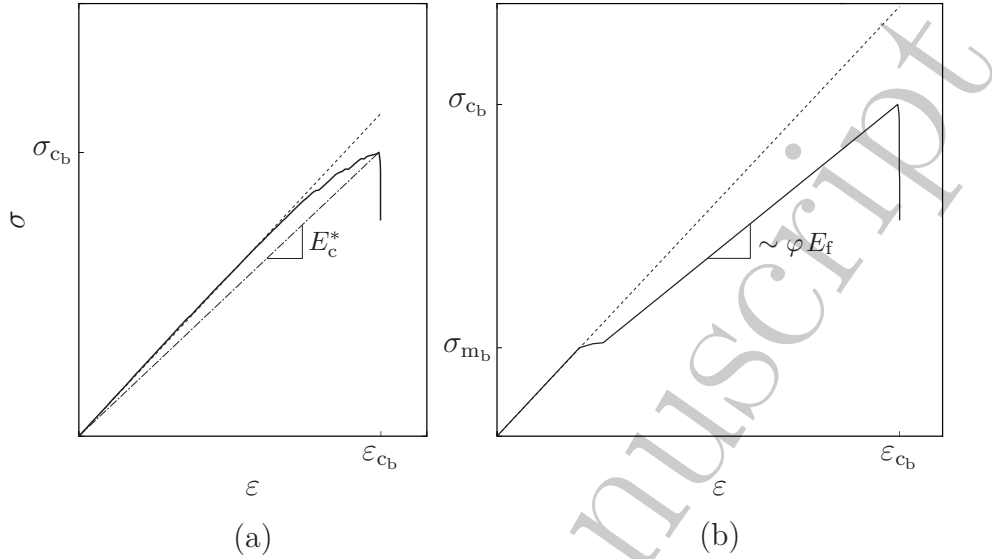


Figure 3: Characteristic stress-strain curve of a unidirectional all-oxide ceramic matrix mini-composite under uniaxial loading (a), schematic stress-strain curve of a unidirectional CMC containing fibres with a (fugitive) coating, after [49, 50] (b). The dashed lines represent fits to the linear region of the stress-strain curves.

An estimate for the matrix stress σ_m at mini-composite failure can be obtained from the relation

$$\sigma_m = E_m^* \varepsilon_{cb}, \quad (5)$$

where E_m^* is the Young's modulus of the damaged matrix phase and ε_{cb} denotes the mini-composites' strain at failure, cf. Fig. 3. Presupposing that no fibre-matrix debonding occurs, i.e. $\varepsilon_f = \varepsilon_m = \varepsilon_{cb}$, the Young's modulus E_m^* of the micro-cracked matrix phase follows from the Rule of Mixtures

$$E_m^* = \frac{E_c^* - \varphi E_f}{1 - \varphi} \quad (6)$$

with the Young's modulus $E_f = 380$ GPa of the undamaged fibres [37]. The Young's modulus E_c^* of the damaged mini-composites was determined from the slope of the secant defined by the true origin of the stress-strain curve, which corresponds to the intersection of the extended linear region of the stress-strain curve with the abscissa, and the point of mini-composite failure associated with ε_{cb} , cf. Fig. 3(a). In the non-linear region of the stress-strain

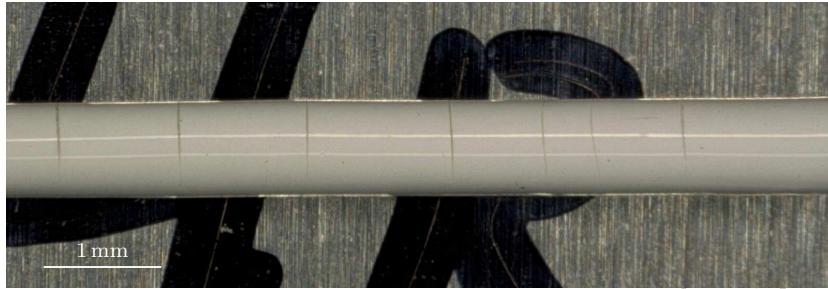


Figure 4: Matrix cracks found on the surface of a mini-composite after tensile failure. The aluminium mounting tab is visible in the background.

curve, the secant modulus is generally higher than the tangent modulus, yielding a conservative estimate for σ_f .

Box plots of the distributions of fibre stress at mini-composite failure are shown in Fig. 5. The means of the distributions are 538.1 MPa (standard deviation 112.4 MPa) for 50 mm gauge length, 467.3 MPa (119.2 MPa) for 125 mm gauge length and 426.2 MPa (69.4 MPa) for 250 mm gauge length. The distributions exhibit moderate variability. Differences between the distributions' means are due to uncertainties in determining the secant moduli of the damaged mini-composites. The notably smaller interquartile range of the fibre stress distribution of specimens with 250 mm nominal gauge length is again attributed to the increased lateral mobility of the longer specimens that leads to reduced scatter.

The weak length dependence of the fibre stress at mini-composite failure suggests that failure of the mini-composites is not solely fibre-induced. The embedded fibres fail at comparatively low stress levels, even if fibre strength degradation due to grain growth during sintering of the mini-composites is considered, cf. Hay et al. [52]. The strain-to-failure of the mini-composites reaches 0.19% at most, which is far lower than the 0.5% strain-to-failure of the filaments [53]. These observations indicate that the mini-composites' failure may be matrix-driven. This assumption is further supported by the correlation of the fibre stress at mini-composite failure and the mini-composites' matrix volume fraction: overall, the mean stress in the fibres at mini-composite failure decreases with increasing matrix volume fraction, as shown in Fig. 6.

An explanation for this trend is provided by the observation that the matrix-rich areas usually exhibit cracks. These matrix cracks possibly already

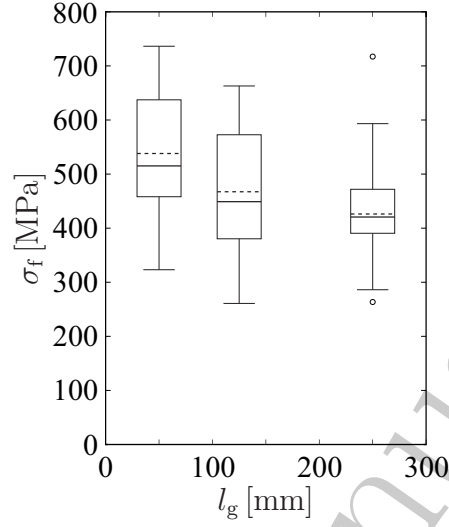


Figure 5: Box plots of the mean fibre stress σ_f at mini-composite failure for different nominal gauge lengths l_g .

form during sintering of the mini-composites.

3.5.2. Effect of sintering-induced matrix shrinkage

During sintering of the mini-composites, the transformation of the dried aqueous slurry into a ceramic matrix goes along with shrinkage. The NextelTM 610 fibres themselves, however, also shrink during the sintering process, mainly as a result of grain growth. Usually, matrix shrinkage is higher than fibre shrinkage, so that the embedded fibres constrain the matrix shrinkage, causing shrinkage stresses. On 14 mini-composites, the length before and after sintering was measured. It was found that, on average, the mini-composites experienced a relative change in length of $\varepsilon_c \approx 0.9\%$ during sintering at 1300°C for one hour.

An estimate for the axial matrix shrinkage strain can be obtained from a one-dimensional balance-of-force analysis, as sketched in Fig. 7. The balance of axial forces F_f in the fibre and F_m in the matrix domain requires

$$F_{m_1} + F_{m_2} - F_f = F_m - F_f = 0, \quad (7)$$

which can be written in the form

$$(1 - \varphi)E_m\varepsilon_m - \varphi E_f\varepsilon_f = 0 \quad (8)$$

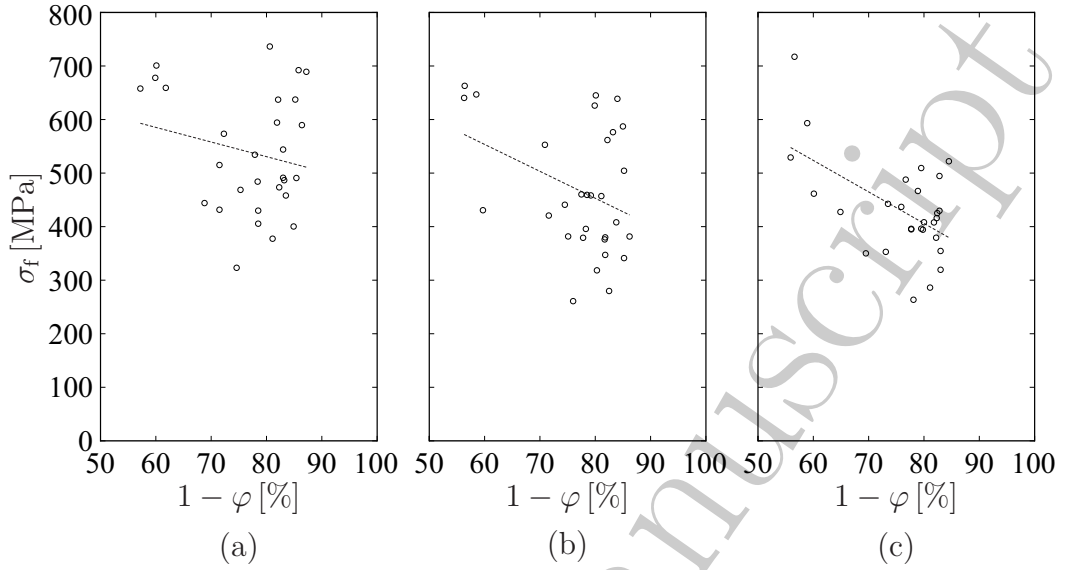


Figure 6: Variation of the mean fibre stress σ_f at mini-composite failure with matrix volume fraction $1 - \varphi$ for (a) 50 mm, (b) 125 mm and (c) 250 mm nominal gauge length. The dashed trend lines represent least-squares fits to the scattered data.

for a given fibre volume fraction φ , the Young's modulus E_f of the fibres and the Young's modulus E_m of the porous matrix phase, which follows from the mini-composite's tensile Young's modulus E_c using the Rule of Mixtures.

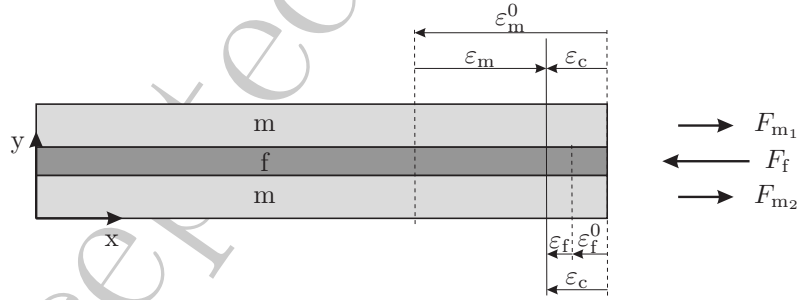


Figure 7: Estimation of sintering-induced overall matrix strain.

Rearranging Eq. (8) leads to the following relation for the overall matrix strain:

$$\varepsilon_m = \frac{\varphi}{1 - \varphi} \frac{E_f}{E_m} \varepsilon_f = \frac{\varphi}{1 - \varphi} \frac{E_f}{E_m} (\varepsilon_c - \varepsilon_f^0), \quad (9)$$

where ε_f^0 denotes the unconstrained shrinkage of the fibres. Length measurements on seven dry fibre roving sections before and after sintering yielded, on average, an unconstrained fibre shrinkage of $\varepsilon_f^0 \approx 0.5\%$ after sintering for one hour at 1300°C . This result compares well with data published by the fibre manufacturer, who reports an unconstrained fibre shrinkage of approximately 0.8% after 15 hours at 1300°C [37].

With a mean matrix Young's modulus of $E_m \approx 52\text{ GPa}$, the fibre Young's modulus $E_f = 380\text{ GPa}$ [37] and a mean fibre volume fraction of $\varphi \approx 23\%$, the overall tensile matrix strain after sintering obtained from Eq. (9) then reads $\varepsilon_m \approx 0.9\%$.

For the above balance-of-force analysis, it is assumed that the mean Young's modulus of the porous matrix phase at room temperature is also valid at the sintering temperature of 1300°C . It is clear that, in reality, the value of the Young's modulus rises from an insignificantly low value to about the room temperature value during the entire sintering process, which involves, amongst others, complex diffusion and creep processes [54]. Thus, the computed result only presents a rough estimate of the overall matrix shrinkage strain. Nevertheless, from the overall mini-composite shrinkage strain of 0.9% , it is obvious that, during the major part of the sintering process, the Young's modulus of the matrix phase is high enough to compress the fibres.

The strain-to-failure of the mini-composites is 0.19% at most. Considering the sintering-induced shrinkage strain and the tensile strain caused by mechanical testing in both the fibres and the porous matrix phase, it becomes clear that cracks are likely to initiate in the matrix phase and that, at the moment of mini-composite failure, globally, the fibres are still under compression.

3.5.3. Effect of mini-composite microstructure

The effect of the matrix phase on the mini-composites' failure behaviour becomes even more apparent when the mini-composites' microstructure, in particular the arrangement of embedded fibres and the presence of matrix-rich areas, are examined. To characterize the mini-composites' microstructure, a nearest neighbour search was performed over all fibre centres on each of the digital images of the 18 bundle cross-sections. From the distances d_{NN} between each fibre centre and the centre of its nearest neighbour, the mean nearest neighbour inter-fibre distance \bar{d}_{NN} was determined for each bundle cross-section.

The dependence of both the corresponding mean fibre stress σ_f at mini-composite failure and the mini-composites' tensile strength σ_{cb} of the 18 bundle cross-sections (two of the mini-composites were damaged prior to testing) on the mean nearest neighbour distance \bar{d}_{NN} of the embedded fibres is illustrated with Fig. 8. Both σ_f and σ_{cb} tend to decrease with an increase in \bar{d}_{NN} .

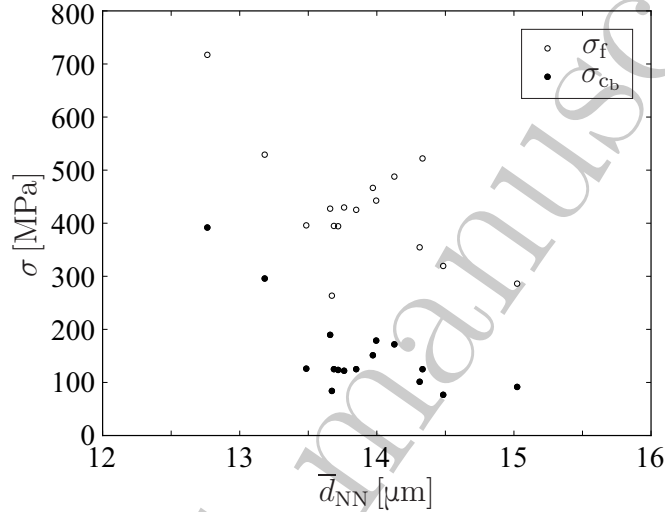


Figure 8: Dependence of the mean fibre stress σ_f at mini-composite failure and the mini-composites' tensile strength σ_{cb} on the mean nearest neighbour distance \bar{d}_{NN} of the embedded fibres. Plotted are the results of 16 investigated mini-composites with 250 mm nominal gauge length.

The mean nearest neighbour inter-fibre distance \bar{d}_{NN} is a very rough descriptor of the mini-composites' microstructure, nevertheless, it can be related to the mini-composites' matrix volume fraction $1 - \varphi$, as shown in Fig. 9. If the fibres are closely spaced, \bar{d}_{NN} takes on low values. In this case, the matrix volume fraction is low and the size of matrix-rich areas in the mini-composites' cross-sections is limited, which results in comparatively high tensile strengths of the mini-composites. High values of \bar{d}_{NN} , on the contrary, indicate high matrix volume fractions and generally large matrix-rich areas, which leads to lower tensile strengths of the mini-composites, cf. Fig. 8.

The continuous curve in Fig. 9 depicts the relation between \bar{d}_{NN} and $1 - \varphi$ that results from an imaginary hexagonal arrangement of fibre centres. This relation was computed in increments of 1 % for matrix area fractions ranging

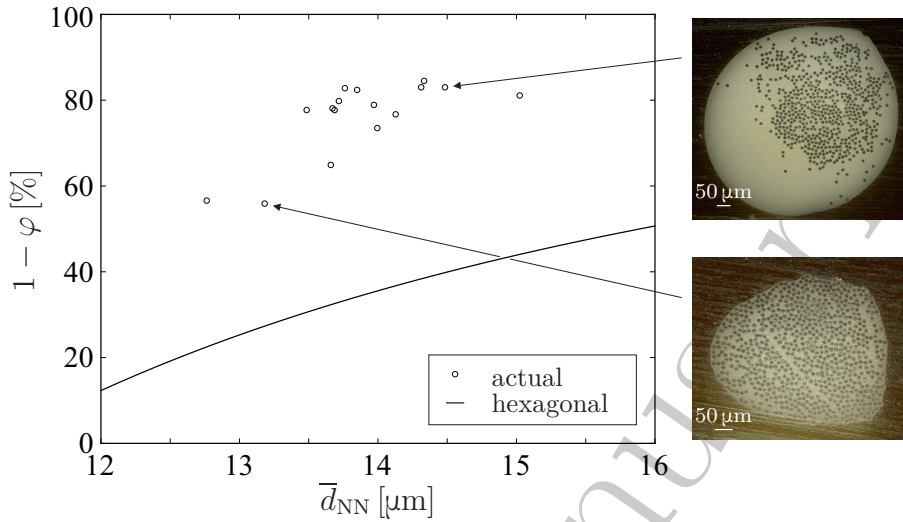


Figure 9: Relation between the mean nearest neighbour distance \bar{d}_{NN} of the embedded fibres and the matrix volume fraction $1 - \varphi$ for both the actual and an imaginary hexagonal fibre arrangement. Circles mark the results of 16 investigated mini-composites with 250 mm nominal gauge length. The inset images show cross-sections of two exemplary mini-composites.

from approximately 10 %, which corresponds to the densest fibre arrangement possible without fibre overlap, to 99 %, assuming a constant fibre diameter of $11.8 \mu\text{m}$ [43]. Only the region of the curve for fixed inter-fibre distances between $12 \mu\text{m}$ and $16 \mu\text{m}$ is shown in Fig. 9.

The graph demonstrates that, for similar matrix fractions $1 - \varphi$, the actual fibre arrangements generally yield lower mean nearest neighbour inter-fibre distances \bar{d}_{NN} than the hexagonal fibre arrangements. This results from the fact that the actual fibre arrangements exhibit non-homogeneous, clustered fibre distributions and, particularly for high matrix fractions, large matrix-rich areas.

In summary, the mini-composites' microstructure affects the formation and propagation of matrix cracks. Mini-composites with large mean nearest neighbour inter-fibre distances exhibit large matrix-rich areas, where long matrix cracks may occur. Accordingly, such mini-composites attain low tensile strengths σ_{cb} , cf. Fig. 8. Mini-composites with shorter mean nearest neighbour inter-fibre distances, in contrast, reach higher tensile strengths, because both the length and quantity of matrix cracks is restricted by the smaller size of inter-fibre matrix regions, where close-by fibres effectively suppress matrix crack formation.

4. Summary and conclusion

Uniaxial tensile tests on all-oxide ceramic matrix mini-composites with highly-porous alumina matrix phase were carried out. The mini-composites failed at comparatively low levels of stress and strain and did not exhibit length-dependent tensile strength properties commonly associated with fibre-dominated failure. The obtained tensile strengths of the mini-composites exhibit large scatter, which is predominantly the result of the strong variation in matrix volume fraction and the non-homogeneous distribution of embedded fibres.

The fibre-parallel shrinkage of the porous matrix phase during sintering is constrained by the dense fibres, causing internal tensile matrix strains. This is particularly critical for mini-composites with high matrix volume fractions and large matrix-rich areas. In these unreinforced matrix areas, comparatively long matrix cracks can form at low applied loads or even during sintering. Under increased tensile loading, these matrix cracks readily propagate and lead to ultimate failure of the mini-composites. Matrix-dominated failure in matrix-rich areas further results in the effect that the mean stress in the fibres at mini-composite failure tends to decrease with increasing matrix volume fraction and increasing mean fibre distance.

5. Acknowledgements

This work was funded by the European Union and the German Federal State of North Rhine-Westphalia as part of the cooperative project ‘CeraMER–Ceramic Materials for Energy Research’. It reflects the personal views of the authors. Support during preparation, mechanical testing and scanning electron microscopy of the ceramic matrix mini-composites provided by F. Flucht, B. Kanka, P. Herzog, M. Rakotomahefa, E. Dietrich, U. Fuchs and L. Chernova, as well as fruitful discussions with K. H. Richter are gratefully acknowledged.

References

- [1] T.J. Lu, Crack Branching in All-Oxide Ceramic Composites, *J. Am. Ceram. Soc.* 79 (1996) 266–274.
- [2] W.-C. Tu, F.F. Lange, A.G. Evans, Concept for a Damage-Tolerant Ceramic Composite with “Strong” Interfaces, *J. Am. Ceram. Soc.* 79 (1996) 417–424.

- [3] F.T. Peirce, Tensile Tests for Cotton Yarns, v.—"The Weakest Link" Theorems on the Strengths of Long and of Composite Specimens, *J. Text. Inst.* 17 (1926) T355–T368.
- [4] H.E. Daniels, The Statistical Theory of the Strength of Bundles of Threads, *Proc. R. Soc. London, Ser. A* 183 (1945) 405–435.
- [5] N.J. Parratt, Defects in Glass Fibers and their Effect on the Strength of Plastic Mouldings, *Rubber Plast. Age* 3 (1960) 263–266.
- [6] B.W. Rosen, Tensile failure of fibrous composites, *AIAA J.* 2 (1964) 1985–1991.
- [7] C. Zweben, B.W. Rosen, A statistical theory of material strength with application to composite materials, *J. Mech. Phys. Solids* 18 (1970) 189–206.
- [8] B. Harris, *Engineering Composite Materials*, second ed., Institute of Metals, London, 1999.
- [9] E. Ryshkewitch, Compression Strength of Porous Sintered Alumina and Zirconia, *J. Am. Ceram. Soc.* 36 (1953) 65–68.
- [10] R.W. Rice, Relation of tensile strength-porosity effects in ceramics to porosity dependence of Young's modulus and fracture energy, porosity character and grain size, *Mater. Sci. Eng. A* 112 (1989) 215–224.
- [11] D.C. Phillips, Long-fibre reinforced ceramics, in: R. Warren (Ed.), *Ceramic-matrix composites*, Blackie and Son, London, 1992, pp. 167–198.
- [12] K.K. Chawla, *Ceramic Matrix Composites*, first ed., Chapman & Hall, London, 1993.
- [13] A.G. Evans, Engineering property requirements for high performance ceramics, *Mater. Sci. Eng.* 71 (1985) 3–21.
- [14] K. Goda, H. Fukunaga, The evaluation of the strength distribution of silicon carbide and alumina fibres by a multi-modal Weibull distribution, *J. Mater. Sci.* 21 (1986) 4475–4480.
- [15] D.M. Wilson, Statistical tensile strength of Nextel™ 610 and Nextel™ 720 fibres, *J. Mater. Sci.* 32 (1997) 2535–2542.
- [16] Y.T. Zhu, W.R. Blumenthal, S.T. Taylor, T.C. Lowe, B. Zhou, Analysis of Size Dependence of Ceramic Fiber and Whisker Strength, *J. Am. Ceram. Soc.* 80 (1997) 1447–1452.
- [17] M.-Y. He, J.W. Hutchinson, Crack Deflection at an Interface between Dissimilar Elastic Materials, *Int. J. Solids Structures* 25 (1989) 1053–1067.
- [18] C.G. Levi, J.Y. Yang, B.J. Dalgleish, F.W. Zok, A.G. Evans, Processing and Performance of an All-Oxide Ceramic Composite, *J. Am. Ceram. Soc.* 81 (1998) 2077–2086.
- [19] J.J. Haslam, K.E. Berroth, F.F. Lange, Processing and properties of an all-oxide composite with a porous matrix, *J. Eur. Ceram. Soc.* 20 (2000) 607–618.

- [20] K. Tushtev, J. Horvath, D. Koch, G. Grathwohl, Deformation and Failure Modeling of Fiber Reinforced Ceramics with Porous Matrix, *Adv. Eng. Mater.* 6 (2004) 664–669.
- [21] H. Cao, M.D. Thouless, Tensile Tests of Ceramic-Matrix Composites: Theory and Experiment, *J. Am. Ceram. Soc.* 73 (1990) 2091–2094.
- [22] H.R. Schwietert, P.S. Steif, A theory for the ultimate strength of a brittle-matrix composite, *J. Mech. Phys. Solids* 38 (1990) 325–343.
- [23] W.A. Curtin, Theory of Mechanical Properties of Ceramic-Matrix Composites, *J. Am. Ceram. Soc.* 74 (1991) 2837–2845.
- [24] W.A. Curtin, Ultimate strengths of fibre-reinforced ceramics and metals, *Composites* 24 (1993) 98–102.
- [25] M.-Y. He, A.G. Evans, W.A. Curtin, The ultimate tensile strength of metal and ceramic-matrix composites, *Acta Metall. Mater.* 41 (1993) 871–878.
- [26] S.L. Phoenix, Statistical issues in the fracture of brittle-matrix fibrous composites, *Compos. Sci. Technol.* 48 (1993) 65–80.
- [27] A.G. Evans, F.W. Zok, The physics and mechanics of fibre-reinforced brittle matrix composites, *J. Mater. Sci.* 29 (1994) 3857–3896.
- [28] N. Lissart, J. Lamon, Damage and failure in ceramic matrix minicomposites: Experimental study and model, *Acta Mater.* 45 (1997) 1025–1044.
- [29] M.E. Walter, G. Ravichandran, M. Ortiz, Computational modeling of damage evolution in unidirectional fiber reinforced ceramic matrix composites, *Comput. Mech.* 20 (1997) 192–198.
- [30] E. Martin, P.W.M. Peters, D. Leguillon, J.M. Quenisset, Conditions for matrix crack deflection at an interface in ceramic matrix composites, *Mat. Sci. Eng. A-Struct.* 250 (1998) 291–302.
- [31] K. Goda, T. Okabe, N. Takeda, A strength reliability model of unidirectional fiber-reinforced ceramic matrix composites by Markov process, *Adv. Compos. Mater.* 15 (2006) 263–285.
- [32] C. Chateau, L. Gélébart, M. Bornert, J. Crépin, D. Caldemaison, C. Sauder, Modeling of damage in unidirectional ceramic matrix composites and multi-scale experimental validation on third generation SiC/SiC minicomposites, *J. Mech. Phys. Solids* 63 (2014) 298–319.
- [33] D.S. Beyerle, S.M. Spearing, F.W. Zok, A.G. Evans, Damage and Failure in Unidirectional Ceramic-Matrix Composites, *J. Am. Ceram. Soc.* 75 (1992) 2719–2725.
- [34] S. Baste, R. El Bouazzaoui, An Experimental Investigation of Stiffness Reduction and Cracks Geometry in a Unidirectional Brittle Matrix Composite, *J. Compos. Mater.* 30 (1996) 282–308.

- [35] R. Naslain, J. Lamon, R. Pailler, X. Bourrat, A. Guette, F. Langlais, Micro/minicomposites: a useful approach to the design and development of non-oxide CMCs, *Composites Part A* 30 (1999) 537–547.
- [36] P.E. Cantonwine, H.N.G. Wadley, The mechanical response of sintered alumina bundles and porous alumina matrix composites, in: J.P. Singh, N.P. Bansal (Eds.), *Advances in Ceramic Matrix Composites IV*, American Ceramic Society, Westerville, 1999, pp. 51–62.
- [37] 3m Corporation, NextelTM Ceramic Textiles Technical Notebook, 3m Ceramic Textiles and Composites, St. Paul, 2004.
- [38] B. Kanka, Ceramic Fibre Composite Material, U.S. Patent 7,919,039, USPTO, Alexandria, 2011.
- [39] Sasol, PURAL[®]/CATAPAL[®] High purity aluminas, Sasol Germany GmbH, Hamburg, 2007.
- [40] B. Kanka, H. Schneider, Aluminosilicate fiber/mullite matrix composites with favorable high-temperature properties, *J. Eur. Ceram. Soc.* 20 (2000) 619–623.
- [41] ASTM Standard C1275-10, Standard Test Method for Monotonic Tensile Behavior of Continuous Fiber-Reinforced Advanced Ceramics with Solid Rectangular Cross-Section Test Specimens at Ambient Temperature, ASTM International, West Conshohocken, 2008.
- [42] ASTM Standard C1557-03, Standard Test Method for Tensile Strength and Young's Modulus of Fibers, ASTM International, West Conshohocken, 2008.
- [43] H. Richter, Numerical modelling of a ceramic matrix composite with porous matrix phase, in: *Proceedings of the 13th ONERA-DLR Aerospace Symposium ODAS 2013*, ONERA, Paris, 2013.
- [44] W.S. Rasband, ImageJ Image Processing and Analysis, U. S. National Institutes of Health, Bethesda, 1997-2014.
- [45] F.E. Grubbs, Procedures for Detecting Outlying Observations in Samples, *Technometrics* 11 (1969) 1–21.
- [46] ASTM Standard E178-80, Standard Practice for Dealing With Outlying Observations, ASTM International, West Conshohocken, 1980.
- [47] S.W. Rust, F.R. Todt, B. Harris, D. Neal, M. Vangel, Statistical Methods for Calculating Material Allowables for MIL-HDBK-17, in: C.C. Chamis (Ed.), *Test Methods and Design Allowables for Fibrous Composites*, American Society for Testing and Materials, Philadelphia, 1989, pp. 136–149.
- [48] J.W. Tukey, *Exploratory data analysis*, Addison-Wesley, Reading, 1977.
- [49] B. Budiansky, J.W. Hutchinson, A.G. Evans, Matrix fracture in fiber-reinforced ceramics, *J. Mech. Phys. Solids* 34 (1986) 167–189.
- [50] R.T. Bhatt, The Properties of Silicon Carbide Fiber Reinforced Silicon Nitride Composites, in: R.A. Bradley, D.E. Clark, D.C. Larsen, J.O. Stiegler

- (Eds.), Whisker- and Fiber-Toughened Ceramics: Proceedings of an International Conference, ASM International, Materials Park, 1988, pp. 199–208.
- [51] M.-Y. He, B.-X. Wu, A.G. Evans, J.W. Hutchinson, Inelastic strains due to matrix cracking in unidirectional fiber-reinforced composites, *Mech. Mater.* 18 (1994) 213–229.
- [52] R.S. Hay, G.E. Fair, T. Tidball, Fiber Strength After Grain Growth in Nextel™ 610 Alumina Fiber, *J. Am. Ceram. Soc.* 98 (2015) 1907–1914.
- [53] A.R. Bunsell, M.-H. Berger, Ceramic fibres, in: J.W.S. Hearle (Ed.), *High-performance fibres*, Woodhead Publishing Ltd., Cambridge, 2001, pp. 239–258.
- [54] C.H. Hsueh, A.G. Evans, R.M. Cannon, R.J. Brook, Viscoelastic stresses and sintering damage in heterogeneous powder compacts, *Acta Metall. Mater.* 34 (1986) 927–936.

Accepted manuscript